Nanoscale

PAPER

View Article Online
View Journal | View Issue

Cite this: *Nanoscale*, 2019, **11**, 13139

Mixed dysprosium-lanthanide nitride clusterfullerenes $DyM_2N@C_{80}$-I_h and $Dy_2MN@C_{80}$-I_h (M = Gd, Er, Tm, and Lu): synthesis, molecular structure, and quantum motion of the endohedral nitrogen atom†

C. Schlesier, F. Liu, * V. Dubrovin, L. Spree, B. Büchner, S. M. Avdoshenko * and A. A. Popov *

Systematic exploration of the synthesis of mixed-metal Dy–M nitride clusterfullerenes (NCFs, M = Gd, Er, Tm, Lu) is performed, and the impact of the second metal on the relative yield is evaluated. We demonstrate that the ionic radius of the metal appears to be the main factor allowing explanation of the relative yields in Dy–M mixed-metal systems with M = Sc, Lu, Er, and Gd. At the same time, Dy–Tm NCFs show anomalously low yields, which is not consistent with the relatively small ionic radius of Tm^{3+} but can be explained by the high third ionization potential of Tm. Complete separation of Dy–Gd and Dy–Er, as well as partial separation of Dy–Lu $M_3N@C_{80}$ nitride clusterfullerenes, is accomplished by recycling HPLC. The molecular structures of $DyGd_2N@C_{80}$ and $DyEr_2N@C_{80}$ are analyzed by means of single-crystal X-ray diffraction. A remarkable ordering of mixed-metal nitride clusters is found despite similar size and electronic properties of the metals. Possible pyramidalization of the nitride clusters in these and other nitride clusterfullerenes is critically analyzed with the help of DFT calculations and reconstruction of the nitrogen inversion barrier in $M_3N@C_{80}$ molecules is performed. Although a double-well potential with a pyramidal cluster structure is found to be common for most of them, the small size of the inversion barrier often leads to an apparent planar structure of the cluster. This situation is found for those $M_3N@C_{80}$ molecules in which the energy of the lowest vibrational level exceeds that of the inversion barrier, including $Dy_3N@C_{80}$ and $DyEr_2N@C_{80}$. The genuine pyramidal structure can be observed by X-ray diffraction only when the lowest vibrational level is below the inversion barrier, such as those found in $Gd_3N@C_{80}$ and $DyGd_2N@C_{80}$. The quantum nature of molecular vibrations becomes especially apparent when the size of the inversion barrier is comparable to the energy of the lowest vibrational levels.

Received 27th April 2019,
Accepted 12th June 2019

DOI: 10.1039/c9nr03593a

rsc.li/nanoscale

Introduction

Nitride clusterfullerenes (NCFs), *i.e.* metallofullerenes with endohedral M_3N clusters, are the most abundant and versatile family of endohedral clusterfullerenes.[1] Since the discovery of the first NCF, $Sc_3N@C_{80}$, in 1999,[2] a large variety of NCFs with various fullerene cage sizes and different metal ions (M = Sc, Y, or lanthanides) have been synthesized.[3] In the M_3N cluster, three M^{3+} ions are located at the vertices of a triangle with the nitride ion N^{3-} in its center. The cluster transfers six electrons to the surrounding carbon cage. The fullerene C_{80}-I_h with a particularly stable hexaanion is the most suitable host for the endohedral species donating six electrons to the cage,[4] and for M = Sc, Y, and lanthanides from Gd to Lu the $M_3N@C_{80}$-I_h NCFs are obtained with the highest yield among other cage sizes. However, when the cluster's size is incommensurate with the C_{80}-I_h cage, as is observed for the early lanthanides from La to Nd with large ionic radii, the distribution of the fullerene sizes shifts to larger cages and the total NCF yield is decreased substantially.[5] For Gd and Tb, although $Gd_3N@C_{80}$-I_h and $Tb_3N@C_{80}$-I_h are still the most abundantly produced Gd- and Tb-NCFs, the large size of the nitride cluster leads to substantial inner strain, which is partially compensated *via* a considerable pyramidalization of the M_3N cluster inside the C_{80}-I_h cage.[3d,6] For smaller metals, the M_3N cluster in

Leibniz Institute for Solid State and Materials Research (IFW Dresden), Helmholtzstrasse 20, 01069 Dresden, Germany. E-mail: f.liu@ifw-dresden.de, s.avdoshenko@ifw-dresden.de, a.popov@ifw-dresden.de

†Electronic supplementary information (ESI) available: Additional details of HPLC separation mass-spectra and X-ray diffraction analysis and optimized coordinates. See DOI: 10.1039/c9nr03593a

$M_3N@C_{80}$-I_h is planar or nearly planar.[3d,6a] Thus, the balance between the ionic radius of the metal and the fullerene size is an important factor influencing the yield and molecular structure of NCFs.[1b,c,6b]

Combining metals of different sizes within one NCF molecule, which would be then dubbed "mixed-metal NCF", is an efficient approach to vary the cluster size and hence alter the product distribution of NCFs. As the ionic radius of Sc is considerably smaller than those of lanthanides, Sc has often been used in the synthesis of binary mixed-metal NCFs. Sc–Y,[7] Sc–Ti,[8] and Sc–V,[9] all Sc–lanthanide binary systems forming NCFs, and even two ternary-metal NCFs, $ScYErN@C_{80}$ and $DyErScN@C_{80}$, have been produced.[10] A number of non-Sc mixed-metal NCFs have also been synthesized, including Ti–Y,[11] Ce–Y,[10e,f] Ce–Lu,[12] Gd–Ho,[13] Gd–Lu,[13,14] Ho–Y,[15] Ho–Lu,[14,15] and Lu–Y.[16] In addition to the alteration of yields and product distribution in comparison with corresponding homometallic NCFs, mixed-metal NCFs may also exhibit different chemical,[7,17] electrochemical,[10e,f,12a] and magnetic properties.[15,18]

The structural diversity of nitride clusters offers a possibility to tune the magnetism of lanthanide-NCFs. The nitride ion in the center of the M_3N cluster bears a large negative charge (the formal charge is $-3e$; the QTAIM analysis gives the value of ca $-1.7e$).[19] Besides, NCF molecules feature rather short lanthanide–nitrogen bonds. The combination of these two factors leads to a large negative charge from a nitride ion in close proximity to a lanthanide and creates a strong axial ligand field (LF) in NCFs, which results in an easy-axis magnetic anisotropy for Ce, Pr, Nd, Tb, Dy, and Ho, and an easy-plane anisotropy for Er and Tm ions.[10i] *Ab initio* calculations performed for Dy-NCFs predict very large LF splitting of Dy^{3+} total momentum (J) states in the range of 1500 cm^{-1},[20] and all three $Dy_xSc_{3-x}N@C_{80}$-I_h NCFs (x = 1–3) were found to be single molecule magnets.[18a,21] However, due to the different cluster compositions and intramolecular Dy⋯Dy interactions, $DySc_2N@C_{80}$-I_h, $Dy_2ScN@C_{80}$-I_h, and $Dy_3N@C_{80}$-I_h exhibit substantially different magnetic properties, which shows that combining Dy with other metals in nitride clusterfullerenes may lead to even more interesting magnetic phenomena, and further exploration of Dy-based mixed-metal NCFs is therefore an important task.

In this work we focus on the binary Dy–metal NCFs with a C_{80}-I_h cage (Fig. 1) and study the influence of the non-Dy metals in the cluster on the synthesis and molecular structure of mixed-metal NCFs, keeping in mind further studies of their magnetic properties, which will be reported elsewhere. As a partner for Dy we have chosen the following elements: Lu as the lanthanide with the smallest ionic radius (Shannon's ionic radius[22] R^{3+} = 0.86 Å); Gd as the largest lanthanide (R^{3+} = 0.94 Å), still favoring the formation of $M_3N@C_{80}$-I_h; and Er (R^{3+} = 0.89 Å) and Tm (R^{3+} = 0.88 Å) as lanthanides with intermediate sizes. Besides, these lanthanides have different magnetic states in NCFs,[10i] and hence their combination with Dy may lead to diverse magnetic properties of mixed-metal NCFs. In the following, we first present a systematic analysis of the influence of the metal on the relative yields of mixed-metal Dy NCFs, and then an analysis of how a combination of Dy with lanthanide ions of different sizes affects the molecular structure and in particular the shape of the trimetal-nitride cluster. In the end we demonstrate how quantum vibrational effects dramatically affect the outcome of the diffraction experiments.

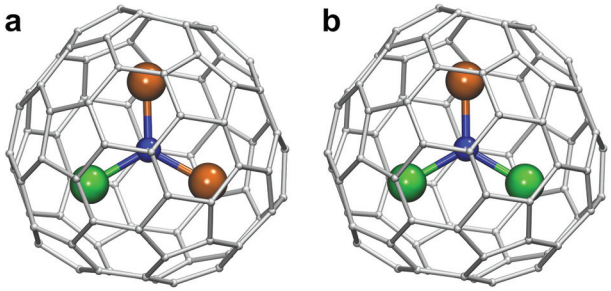

Fig. 1 $DyM_2N@C_{80}$ (a) and $Dy_2MN@C_{80}$ (b) molecules based on the C_{80}-I_h carbon cage isomer. Dy is depicted in green, the lanthanide M in dark orange, N in blue and carbon atoms in light gray.

Synthesis

The synthesis of all mixed-metal EMFs in this work was performed following the same protocol. Graphite rods were core-drilled and filled with a mixture of Dy/M (1 : 1 molar ratio), graphite, and melamine as a source of nitrogen. The molar ratio Dy : M : N : C was kept at 1 : 1 : 10 : 15. The rods were evaporated under a He atmosphere (200 mbar) using a current of 100 A. Current phases were 30–60 s long, followed by a cooling period. As only the cathode is evaporated in the arc-discharge, the polarity of the rods was changed between the phases to ensure evaporation of both electrodes. The soot produced was collected, washed with acetone and extracted with CS_2 for 20 hours. Then the CS_2 was evaporated, the fullerene extract was redissolved in toluene, characterized by analytical HPLC and LDI mass-spectrometry, and then separated by multi-step HPLC as described below.

Comparison of the binary Dy–M NCF systems

Fig. 2 compares chromatograms of the raw fullerene extracts obtained for Dy–Gd, Dy–Er, Dy–Tm, and Dy–Lu systems. For all systems, chromatograms are dominated by a strong peak with a retention time near 32 min, which based on our previous experience with NCF synthesis is assigned to the mixture of $Dy_xM_{3-x}N@C_{80}$-I_h NCFs (x = 0–3). The peak next to it with a retention time of *ca.* 34 min is assigned to NCFs with a C_{80}-D_{5h} cage, whereas the peaks at longer retention times are NCFs with larger cages. Note that the relative yield of NCFs with larger cages is the highest in the Dy–Gd system. Nonetheless, as discussed in the introduction, NCFs with C_{80}-I_h cages are produced with the highest yield, and in the following we will

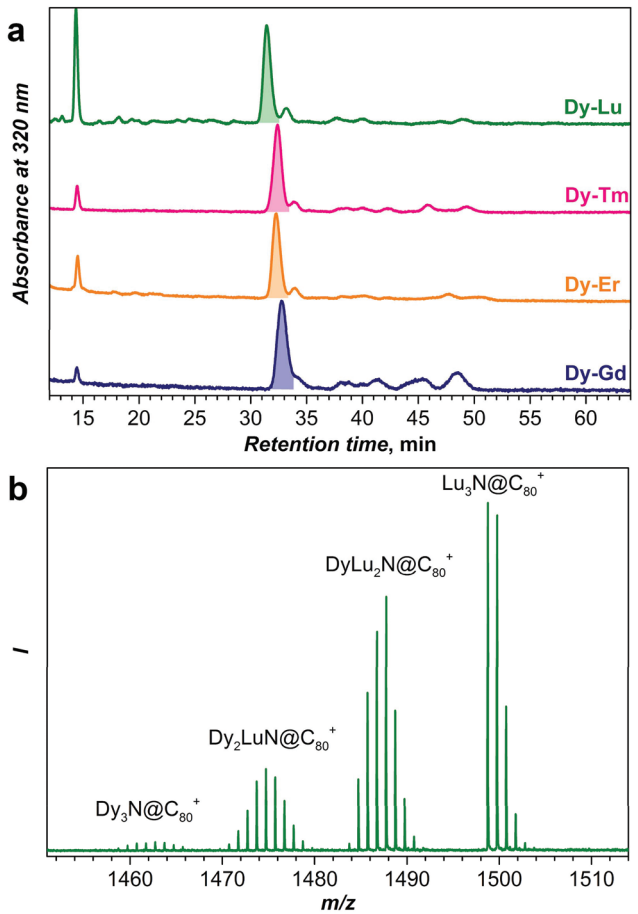

Fig. 2 (a) HPLC chromatograms of raw fullerene extracts obtained in the Dy–Lu, Dy–Er, Dy–Tm, and Dy–Gd NCF syntheses (analytical BuckyPrep column, toluene as the eluent, 40 °C, 1.6 mL min^{-1}). The sharp peak at 14–15 min is attributed to C_{70}, the main NCF fractions comprising $Dy_xM_{3-x}N@C_{80}$-I_h (x = 0–3) eluted at 31–34 min (shaded with the corresponding color). (b) LDI mass-spectrum of the $Dy_xLu_{3-x}N@C_{80}$ (x = 0–3) fraction measured in the positive ion mode.

focus only on this cage isomer. Unless otherwise stated, from here on we will omit the cage symmetry designation and assume C_{80} to be C_{80}-I_h.

For an equimolar mixture of Dy and a metal M in the starting material (*i.e.* the Dy : M molar ratio is 1 : 1), the ratio of Dy_3N : Dy_2MN : DyM_2N : M_3N clusters in the synthesized NCF mixture should be 1 : 3 : 3 : 1 given that the product ratio follows binominal statistical distribution without a bias for any of the metals. However, the studies of mixed-metal EMFs showed that the ratio of the cluster composition rarely follows the expected statistical distribution.[2,10e,h,23] The use of an array of metals in combination with Dy in this work enables a systematic study of this phenomenon. As a method for fast analysis of the sample composition, here we use laser-desorption ionization mass-spectrometry (LDI-MS). Although LDI-MS can hardly be applied for a quantitative estimation of an arbitrary fullerene mixture because of different ionization efficiencies, it is known that all $M_3N@C_{80}$ NCFs have almost identical oxidation potentials independent of the metals in the cluster,[1d] and hence similar ionization efficiency in the positive ion mode can be expected for all $M_3N@C_{80}$ molecules studied in this work. Thus, the analysis of the LDI-MS intensities should give if not the quantitative estimation of the relative yield in each mixed-metal system, but at least a trend in the values.

Fig. 2b and 3 show mass-spectra of the $M_3N@C_{80}$ fraction for each Dy–M system. As Dy and Lu have sufficiently different atomic masses, the peaks of all four $Dy_xLu_{3-x}N@C_{80}$ (x = 0–3) species can be easily distinguished in the mass spectrum (Fig. 2b). For other Dy–M systems, the relatively broad isotopic distribution and closer atomic masses result in overlapping spectral patterns, which still can be used for the estimation of the sample composition by matching with theoretical isotopic distributions for the involved species (Fig. 3 and S1†). The relative yield of a given $Dy_xM_{3-x}N@C_{80}$ compound in the Dy–M mixed system referred to the yield of $Dy_3N@C_{80}$ is then computed as a ratio of the total LDI-MS intensities of $Dy_xM_{3-x}N@C_{80}$ to $Dy_3N@C_{80}$ (Table S1†). The relative yield of $Dy_3N@C_{80}$ in each system is then considered to be equal to 1. The relative yields estimated from mass-spectral data are plotted in Fig. 4 along with the data on the Dy–Sc system studied in our group earlier. A strong deviation from the binominal statistical distribution (1 : 3 : 3 : 1) is found in all binary systems. Note that the following discussion is based on the relative yields of NCFs in mixed-metal systems. The absolute yield of $Dy_3N@C_{80}$ varies in different mixed-metal systems, and hence Fig. 4 and the data in Table S1† do not give an estimation of the total yields of NCFs. We do observe a general trend that the absolute yield of $Dy_3N@C_{80}$ in the mixed-metal systems with a small second metal (Sc or Lu) is considerably lower than the absolute yield of $Dy_3N@C_{80}$ in a mixed-metal system with bigger metals (such as Gd), but a precise estimation of the absolute yields is not possible due to the small amount of EMFs produced by arc-discharge synthesis and is not discussed further.

A clear tendency of the relative yield variation with the size of the metal is seen in Fig. 4. Sc with the smallest ionic radius gives the highest relative yields of $Dy_2MN@C_{80}$, $DyM_2N@C_{80}$, and $M_3N@C_{80}$. The ratio of Dy_2ScN and $DySc_2N$ is 0.5 instead of the expected 1, and the ratio of $DySc_2N$ and Sc_3N is 1.5 instead of 3. Clearly, under identical conditions, Sc is much more predisposed to the formation of $M_3N@C_{80}$ than Dy. In the Dy–Lu and Dy–Er systems the relative yields of $DyM_2N@C_{80}$ and $M_3N@C_{80}$ are also much higher than the expected 3 to 1, respectively, but smaller than those for Sc analogs. The decrease of the relative yield of mixed-metal species is in line with the increase of the ionic radii from Sc (0.75 Å) to Lu (0.86 Å) to Er (0.89 Å). For Gd (0.94 Å), whose ionic radius is higher than that of Dy (0.91 Å), the situation is reversed, and the relative yields of Dy_2GdN, $DyGd_2N$, and Gd_3N species decrease with the number of Gd ions in the cluster. Thus, a simple conclusion might be drawn based on these data: the metals with an ionic radius smaller than Dy are more favorable for NCF formation, whereas the metals with a bigger ionic radius are less predisposed to NCF formation. However,

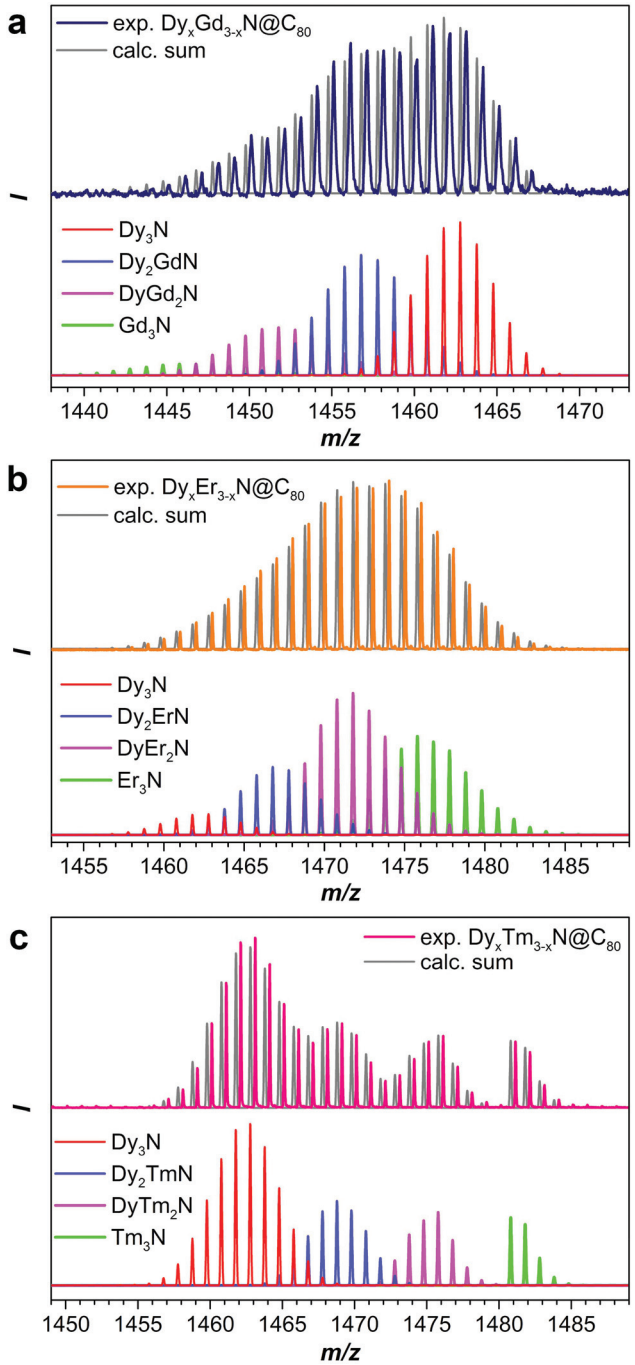

Fig. 3 LDI mass-spectra of the $Dy_xM_{3-x}N@C_{80}$-I_h (x = 0–3) fractions measured in positive ion mode: (a) M = Gd; (b) M = Er; and (c) M = Tm. Each panel contains overlaid calculated mass-spectra of individual $Dy_xM_{3-x}N@C_{80}$ molecules (bottom) and a comparison of the experimental and calculated mass-spectra of the whole fraction (top). For the sake of a clearer comparison experimental mass-spectra are shifted to higher masses by 0.3 a.m.u.

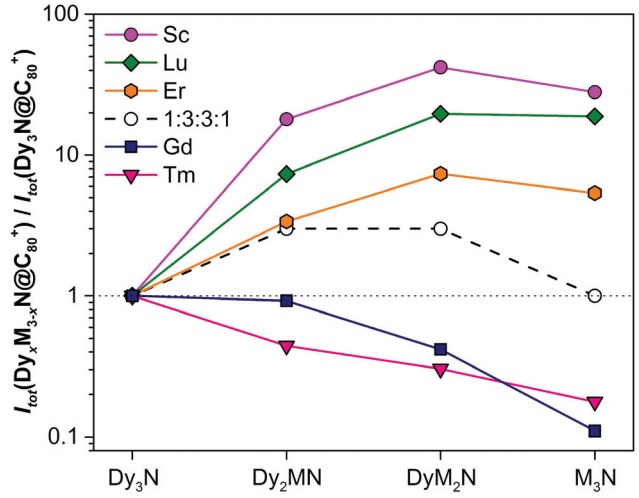

Fig. 4 Relative yields of $Dy_xM_{3-x}N@C_{80}$-I_h NCFs (M = Sc, Lu, Er, Tm and Gd) in each mixed-metal system determined from LDI-MS intensities and normalized to the intensity of $Dy_3N@C_{80}$-I_h (note that the data are plotted in a logarithmic scale). Also shown are the yields expected for the binominal statistical distribution of metals in the nitride cluster (1 : 3 : 3 : 1). Numerical data used to prepare this plot can be found in Table S1 in the ESI.† Note that the absolute yield of $Dy_3N@C_{80}$ varies in different mixed-metal systems.

the data for the Dy–Tm system shows that the ionic radius is not the only factor affecting the yield of NCFs.

With an ionic radius of 0.88 Å, Tm^{3+} is slightly smaller than Er^{3+} and considerably smaller than Dy^{3+}, but the distribution of Dy–Tm NCFs points to the higher preference for Dy *versus* Tm for NCF formation. The relative yields of $Dy_2TmN@C_{80}$ and $DyTm_2N@C_{80}$ are even smaller than those of $Dy_2GdN@C_{80}$ and $DyGd_2N@C_{80}$. We suggest that the reason for the anomalously low yield of Dy–Tm NCFs lies in the electronic properties of Tm, particularly in its third ionization potential. It is known that in monometallofullerenes some lanthanides are divalent, whereas others adopt a trivalent state. Shinohara *et al.* demonstrated that the valence states of lanthanides in EMFs correlate well with their third ionization potentials (IP_3, see also Fig. S2†).[24] The metals with a large IP_3 exceeding 23 eV, namely Sm, Eu, Tm, and Yb, donate only two electrons to the fullerene cage and remain divalent, whereas IP_3 values of La, Ce, Pr, Nd, Gd, Tb, Dy, Ho, Er, and Lu are below the threshold of 23 eV. These lanthanides are ionized by a hosting fullerene cage to their trivalent state. Furthermore, the lanthanides with an IP_3 below 23 eV form nitride clusterfullerenes (in which the valence state of the metal is also trivalent), whereas clusterfullerenes of Sm, Eu, and Yb are not known. Tm is the only lanthanide able to adopt a variable valence state in EMFs, a divalent state in monometallofullerenes and a trivalent state in NCFs.[25] Presumably, the high IP_3 value of Tm still takes its toll in NCF formation by lowering the synthetic yields of $Dy_2TmN@C_{80}$, $DyTm_2N@C_{80}$, and $Tm_3N@C_{80}$.

As the yield of Dy–Tm NCFs is too low, further accumulation and separation of $Dy_xM_{3-x}N@C_{80}$ NCFs were only performed for M = Gd, Er, and Lu. $Dy_xM_{3-x}N@C_{80}$ NCFs with the same fullerene cage show very similar retention behavior, and their separation requires several steps of recycling HPLC. Fig. 5 shows plots of recycling chromatograms for all three mixtures

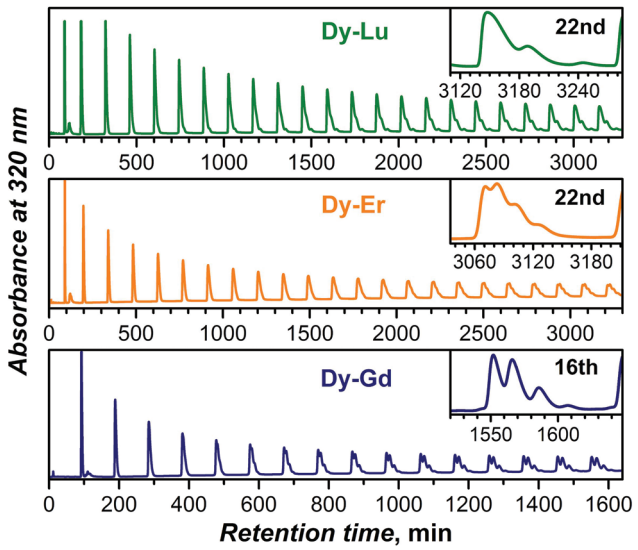

Fig. 5 Recycling HPLC chromatograms of $Dy_xM_{3-x}N@C_{80}$ mixtures (x = 0–3) for M = Lu, Er, and Gd (semipreparative BuckyPrep column, toluene as the eluent, 25 °C, flow rate: 1.0 mL min^{-1}). Insets show an enlarged fragment of the chromatogram obtained at the 22nd cycle (Dy–Lu and Dy–Er system) or 16th cycle (Dy–Gd system).

obtained for the main $Dy_xM_{3-x}N@C_{80}$ fractions highlighted in Fig. 2 at the first step (Fig. S3–S8† show further separation details). The Dy–Gd system offers the most straightforward separation among the three. Clear resolution into four components (with Dy_3N, Dy_2GdN, $DyGd_2N$, and Gd_3N clusters) can be seen after 16 cycles. For the $Dy_xEr_{3-x}N@C_{80}$ mixture, a similar level of separation requires at least twice more cycles (Fig. 5 and S5†), which further complicates the separation not only because of the increased time demands, but also because of the overlap of the fastest fractions at the nth cycle with the slowest fractions at the $(n-1)$th cycle. Surprisingly, the $Dy_xLu_{3-x}N@C_{80}$ mixture proved to be the most difficult to separate despite the largest difference in the ionic radii of Dy^{3+} and Lu^{3+}. Whereas the resolution of the $Dy_3N@C_{80}$ and $Dy_2LuN@C_{80}$ HPLC peaks is possible after 25 and 40 cycles, respectively (Fig. 5 and S7†), the retention times of $Lu_3N@C_{80}$ and $DyLu_2N@C_{80}$ are so close that their separation cannot be accomplished even after 70 cycles (Fig. S7 and 8†).

In summary, multistep recycling HPLC allowed the isolation of $Dy_2GdN@C_{80}$, $DyGd_2N@C_{80}$, $DyEr_2N@C_{80}$, and $Dy_2ErN@C_{80}$ in high compositional purity exceeding 90–95% based on mass-spectroscopic analysis (see Fig. S4, S6, and S8†). The retention behavior of $Dy_2LuN@C_{80}$, $DyLu_2N@C_{80}$ and $Lu_3N@C_{80}$ was found to be too similar to offer efficient separation without a substantial loss of the material. $Dy_2LuN@C_{80}$ could be separated to *ca.* 90% purity (the sample also contained *ca.* 10% $DyLu_2N@C_{80}$ and *ca.* 3% $Lu_3N@C_{80}$), whereas the separation of $DyLu_2N@C_{80}$ from $Lu_3N@C_{80}$ is hardly possible and was aborted when the relative content of the two NCFs in the sample was *ca.* 1 : 1.35. Note that earlier we have had similar difficulties with the separation of the $Ho_xLu_{3-x}N@C_{80}$ NCFs.[15]

Spectroscopic characterization

Since the absorption of UV and visible light by EMFs are dominated by the $\pi \rightarrow \pi^*$ transition of the fullerene cage, UV-Vis absorption spectra of $M_3N@C_{80}$ NCFs are known to be very similar irrespective of the endohedral M_3N cluster, unless the latter also includes Sc atoms, in which case the differences between spectra are more pronounced.[1d,10g,k,16,23] Indeed, UV-Vis absorption spectra of the Dy–Gd and Dy–Er $M_3N@C_{80}$ families also follow this trend and have an almost identical appearance with absorptions near 325, 410, and 555 nm and 3–4 weak features in the long-wavelength range at 620–720 nm (Fig. 6). However, more detailed analysis of the lowest-energy part of the spectra shows a small but systematic variation of the peak energies. Upon going from $Gd_3N@C_{80}$ to $Dy_3N@C_{80}$ and then to $Er_3N@C_{80}$ *via* corresponding mixed-metal counterparts (*i.e.* with a gradual decrease of the cluster size), absorption energies shift to shorter wavelengths (higher energies) from 708/675 nm in Gd_3N to 695/665 nm in $Er_3N@C_{80}$ (Fig. 6, inset). Although the HOMO and LUMO of non-Sc $M_3N@C_{80}$-I_h NCFs are mainly localized on the fullerene cage, a small contribution of the metal cluster to the LUMO was also established,[26] which is presumably responsible for the blue-shift of the lowest energy transitions with the decrease of the cluster size.

Single-crystal analysis and molecular structures

The molecular structures of $DyEr_2N@C_{80}$ and $DyGd_2N@C_{80}$ were established by single-crystal X-ray diffraction using syn-

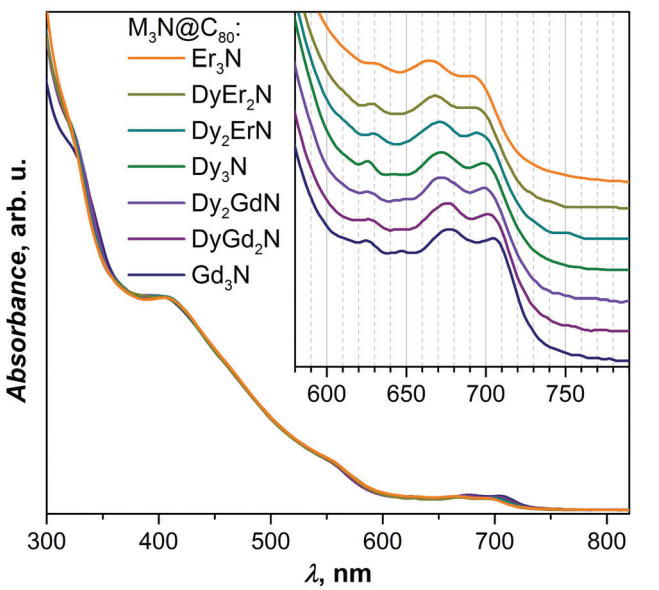

Fig. 6 Overlaid UV-Vis absorption spectra of isolated $M_3N@C_{80}$ NCFs measured in toluene solution at room temperature. The inset shows an expansion of the low-energy part; the spectra are offset for easier comparison.

chrotron radiation at BESSY II of the Helmholtz-Zentrum Berlin.[27] Single crystals suitable for diffraction analysis were obtained by co-crystallization of $DyEr_2N@C_{80}$ and $DyGd_2N@C_{80}$ with Ni^{II}(OEP) (OEP = octaethylporphyrin). The $DyM_2N@C_{80}{\cdot}Ni^{II}$(OEP) fragments of $DyGd_2N@C_{80}{\cdot}Ni^{II}$(OEP)·2($C_6H_6$) and $DyEr_2N@C_{80}{\cdot}Ni^{II}$(OEP)·2($C_6H_6$) crystals are shown in Fig. 7. As in many other $M_3N@C_{80}{\cdot}Ni^{II}$(OEP) co-crystals, both fullerene cages and Ni^{II}(OEP) molecules are well ordered with their nearest cage carbon–Ni contacts of 2.81–2.82 Å.

In the icosahedral C_{80}-I_h cage the M_3N cluster has many energetically equivalent positions, which result in the free rotation of the cluster inside the cage in solution and may lead to disorder in the crystalline phase; even stronger disorder may be expected for the mixed-metal NCFs due to the overlap of different metal positions in the cluster. The unique advantage of co-crystallization with Ni^{II}(OEP) for NCFs is that not only the fullerene cage, but also the endohedral cluster is often well ordered in the crystal.[6b,10c,j] The plane of the M_3N cluster is usually perpendicular to the porphyrin plane of the Ni^{II}(OEP) molecule, two metals face the Ni^{II}(OEP)-coordinated part of the cage, and the third metal is oriented towards the opposite side of the fullerene cage (Fig. 7). In the $MSc_2N@C_{80}{\cdot}Ni^{II}$(OEP) and $M_2ScN@C_{80}{\cdot}Ni^{II}$(OEP) co-crystals, the position farthest from the porphyrin is always adopted by the larger lanthanide, whereas one or two Sc atoms are oriented closer to the Ni^{II}(OEP). Likewise, in the $CeLu_2N@C_{80}{\cdot}Ni^{II}$(OEP)·2$C_7H_8$ crystal ($CeLu_2N@C_{80}$-I_h is the only non-Sc mixed-metal NCF studied by single-crystal X-ray diffraction before this work), the larger Ce atom is located further away from the Ni^{II}(OEP), and smaller Lu atoms are located closer to the porphyrin.[12b] We have recently studied the ordering of the endohedral cluster in $Sc_3N@C_{80}$ and $YSc_2N@C_{80}$ by Ni^{II}(OEP) theoretically and found that the ordering can be explained by simple electrostatic consideration based on the distribution of the electrostatic potential in the molecules.[28] The importance of the electrostatic potential distribution for co-crystallization with Ni^{II}(OEP) has also been reported for some other empty and endohedral fullerenes.[29] Furthermore, the study of $YSc_2N@C_{80}$ showed that different metals (Y and Sc in that case) cause slightly different distribution of electrostatic potentials outside the fullerene cage, which may lead to a further alignment of the mixed-metal clusters.

Although in the $DyM_2N@C_{80}$ NCFs studied in this work the difference of the ionic sizes of metals is not as pronounced as in the already reported mixed-metal NCFs, co-crystallization with Ni^{II}(OEP) still results in remarkable ordering of the nitride clusters. In $DyGd_2N@C_{80}{\cdot}Ni^{II}$(OEP), the single Dy ion is

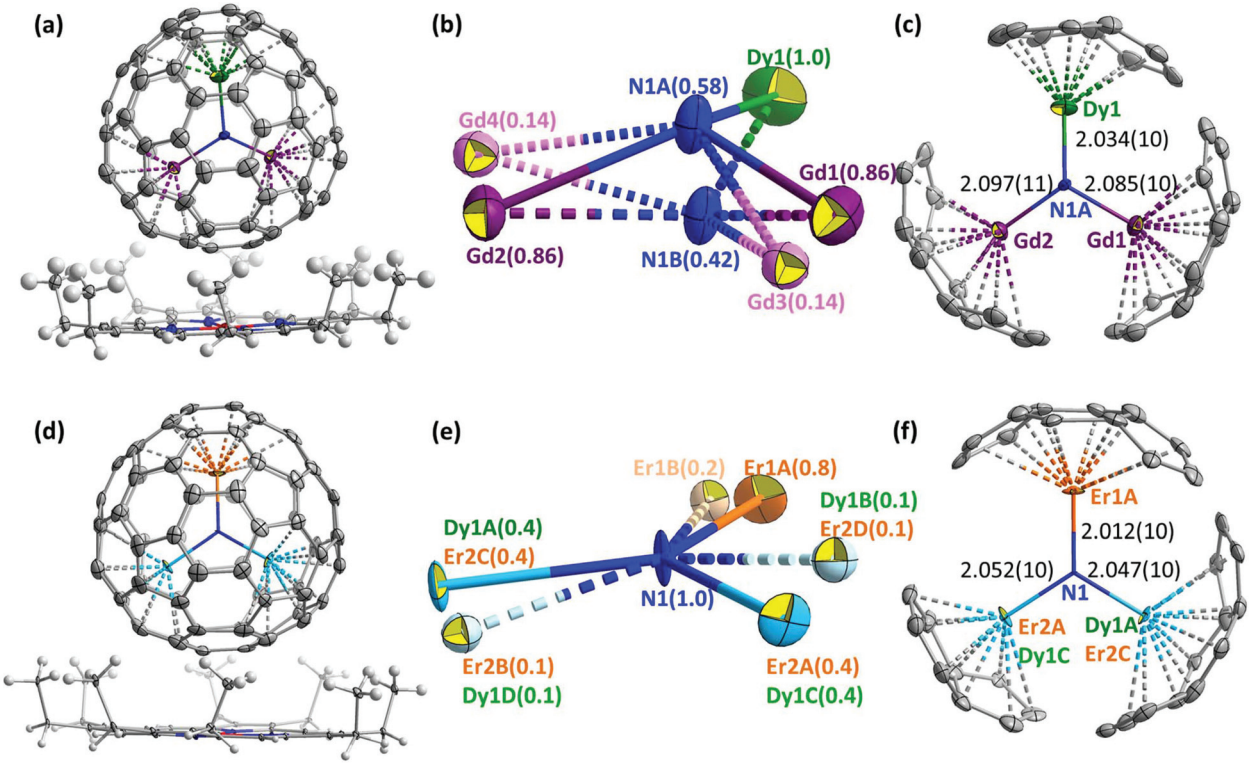

Fig. 7 (a) Crystal structure of $DyGd_2N@C_{80}{\cdot}Ni^{II}$(OEP)·2($C_6H_6$). Solvent molecules are omitted for clarity and only the main site of the $DyGd_2N$ cluster is shown; (b) all sites of the $DyGd_2N$ cluster in the crystal; the site occupancies are noted in parentheses; (c) the main $DyGd_2N$ site and coordinated fragment of the fullerene cage; also shown are metal–nitrogen bond lengths (in Å). (d) Crystal structure of $DyEr_2N@C_{80}{\cdot}Ni^{II}$(OEP)·2($C_6H_6$). Solvent molecules are omitted for clarity and only site A of the $DyEr_2N$ cluster is shown. (e) All sites of the $DyEr_2N$ cluster in the crystal; the site occupancies are noted in parentheses and (f) the $DyEr_2N$ site A and coordinated cage carbons and metal–nitrogen bond lengths (in Å). The displacement parameters are shown at the 30% probability level.

fully ordered and is located remotely from the Ni^{II}(OEP), whereas Gd atoms are refined to two sites with occupancies of 0.86 and 0.14 (Fig. 7). Two sites with occupancies of 0.58 and 0.42 located at a distance of 0.91(2) Å from each other are refined for nitrogen. For the main site of the $DyGd_2N$ cluster shown in Fig. 7c, the bond lengths are 2.034(10), 2.085(10), and 2.097(11) Å for Dy1–N1A, Gd1–N1A, and Gd2–N1A, respectively, and the bond angles at nitrogen N1A are: ∠Dy1N1AGd1 = 116.8(5)°, ∠Dy1N1AGd2 = 118.0(5)°, and ∠Gd1N1AGd2 = 111.1(5)° with a sum of 345.9°. The geometry of the minor site of the $DyGd_2N$ cluster shown in Fig. S9b† has a small deviation from the major site geometry. Splitting of the nitrogen positions and deviation of the sum of ∠MNM' angles from 360° indicate that the $DyGd_2N$ cluster inside the C_{80}-I_h cage is pyramidal.

In $DyEr_2N@C_{80}{\cdot}Ni^{II}$(OEP), two sites of $DyEr_2$ are well recognized with occupancies of 0.8 and 0.2. The Er1 atom is located far from the Ni^{II}(OEP). The Er2 and Dy1 atoms are overlapped and face the porphyrin-coordinated site of the cage. Thus, in both $DyGd_2N@C_{80}{\cdot}Ni^{II}$(OEP) and $DyEr_2N@C_{80}{\cdot}Ni^{II}$(OEP) crystals, the position farthest from the porphyrin is occupied by the smaller lanthanide (Dy or Er), in contrast to the situation described earlier for MSc_2N,[10c,d,j,21b,30] M_2ScN,[10j,21c] and $CeLu_2N$[12b] clusters.

The nitrogen in the $DyEr_2N$ cluster is nearly located on the plane of $DyEr_2$ with an out of plane displacement of 0.05(1) Å. The nitrogen ellipsoid is strongly elongated perpendicular to the $DyEr_2$ plane. Due to the overlap of Dy1 and Er2, estimation of the Dy–N bond distance cannot be very accurate. The bond lengths are 2.012(10), 2.047(10), and 2.052(10) Å for Er1A–N1, Dy1A/Er2C–N1, and Er2A/Dy1C–N1, respectively. Thus, the average of Dy1–N and Er2–N bond lengths is longer than the Er1–N distance in agreement with the larger ionic radius of Dy. The bond angles at the nitrogen site are: ∠Dy1A/Er2CN1Er1A = 123.1(5)°, ∠Dy1A/Er2CN1Er2A/Dy1C = 115.1(5)°, and ∠Er1AN1Er2A/Dy1C = 121.6(5)°, with a sum of 360°.

Note that Dy/Gd or Dy/Er are crystallographically rather similar and it is hardly possible to distinguish them unambiguously. For $DyGd_2N@C_{80}$, our assignment shown in Fig. 7b is based on the higher electron density at the Dy1 site when compared to both Gd sites. Besides, the shorter Dy–N and longer Gd–N bond distances determined with this assignment (Fig. 7c) are in good agreement with the larger ionic radius of Gd^{3+} in comparison with that of Dy^{3+}. Likewise, assignment of the Er1(A/B) site in $DyEr_2N@C_{80}$ is also based on the higher electron density at that position and on the reasonable distribution of the metal–nitrogen bond lengths following the expected shorter Er–N and longer Dy–N bonds (Fig. 7f). However, current experimental data do not allow us to exclude some overlap (in the range of 10%) between Gd and Dy positions in $DyGd_2N@C_{80}$ or a further overlap between Er1 and Dy in $DyEr_2N@C_{80}$.

The pronounced pyramidalization of the $DyGd_2N$ cluster and the nearly planar shape of the $DyEr_2N$ cluster are in line with the crystallographic studies of other $M_3N@C_{80}$ molecules.[6b] The shape of the nitride cluster in NCFs depends on the match between the size of the cluster and the cage size. The most stable form of the cluster is planar, and it is realized in those NCFs which offer sufficient inner space for the cluster. If the cage size is fixed as in the $M_3N@C_{80}$ series considered here, the increase of the metal size leads to the inner strain of the structure. The geometrical parameters of the M_3N cluster have a certain flexibility, and the M–C and M–N bonds may become shorter in comparison with their optimal values, to maintain the planarity of the cluster. However, when the planarity of the cluster requires shortening of the M–N and M–C bonds beyond a certain threshold, the nitrogen atom is pushed out of the M_3 plane and the cluster adopts a pyramidal shape instead.

Table 1 summarizes the Gd–N, Dy–N, Er–N, and Lu–N bond lengths in different $M_3N@C_{80}$ NCFs determined by single-crystal X-ray diffraction studies. The average M–N bond length in $Lu_3N@C_{80}$, $Er_3N@C_{80}$, and $Dy_3N@C_{80}$ is in the range of 2.04–2.05 Å, although the ionic radii of Dy^{3+} and Lu^{3+} are different by 0.05 Å. The Er_3N and Lu_3N clusters are nearly planar, whereas for Dy_3N the experimental data allow two alternative interpretations: one suggests a planar cluster and a single nitrogen site, in which the thermal ellipsoid is strongly elongated in the out-of-plane direction.[31] A more recent interpretation of the same diffraction data suggests splitting of the nitrogen position between two sites leading to a pyramidal Dy_3N cluster.[6b] In $Gd_3N@C_{80}$, a further increase of the metal size results in an average Gd–N bond length of 2.08 Å, and the Gd_3N cluster has to adopt a pyramidal configuration in $M_3N@C_{80}$.[6a]

Note that Dy–N bonds of 2.0–2.1 Å determined for Dy-containing NCFs are much shorter than typical Dy–N bond lengths. Fig. 8 shows the distribution of 5369 Dy–N bond lengths in molecular Dy compounds retrieved from the Cambridge Structural Database (CSD). The shortest non-fullerene Dy–N bond reported to date is 2.14 Å long,[32] whereas in a majority of such compounds the Dy–N bond lengths are in the range of 2.3–2.7 Å.[33] The short Dy–N bond length is an indication of significant strain experienced by lanthanide M_3N clusters encapsulated inside the C_{80} fullerene cage.

Mixed-metal nitride clusters allow redistribution of the bond lengths and hence a partial release of the strain. Geometrical parameters of MSc_2N and M_2ScN clusters (M = Gd, Dy, Er) clearly illustrate this effect. M–N bonds in $MSc_2N@C_{80}$ NCFs are considerably longer than the M–N bonds in the corresponding $M_3N@C_{80}$ molecules (Table 1). In $M_2ScN@C_{80}$ (M = Gd, Dy) the M–N bond lengths become shorter than those in MSc_2N clusters and approach the values found in $M_3N@C_{80}$ molecules. Yet, both MSc_2N and M_2ScN clusters are planar for all lanthanides studied so far.[10c,d,j,21b,c,30] In $DyGd_2N@C_{80}$, the length of the Gd–N bonds is comparable to those in Gd_3N, and the Dy–N bond is even somewhat shorter than that in $Dy_3N@C_{80}$. Thus, both Gd–N and Dy–N bonds reached their shortest threshold values, and the $DyGd_2N$ cluster has to become pyramidal to release the strain further. For $DyEr_2N$ the situation is less obvious because of the overlapped Dy/Er positions, which make the bond

Table 1 Metal–nitrogen bond lengths (Å) in selected $M_3N@C_{80}$-I_h molecules from X-ray diffraction and DFT calculations

	Gd–N	Dy–N	Er–N	Lu–N
$R(M^{3+})$[a]	0.94	0.91	0.89	0.86
X-ray diffraction				
M_3N	**Gd_3N** (ref. 6*a*)	**Dy_3N** (ref. 6*b* and 31)	**Er_3N** (ref. 6*b*)	**Lu_3N**
	2.038(8)	2.004(8)	2.046(3)	*2.050 (av)*[b] (ref. 34)
	2.085(4)	2.068(6)	2.059(3)	*2.032 (av)*[b] (ref. 35)
	2.117(5)	2.055(7)	2.028(3)	*2.041 (av)*[b] (ref. 3*c*)
	2.080 (av)[b]	*2.042 (av)*[b]	*2.044 (av)*[b]	
MSc_2N	**$GdSc_2N$** (ref. 10*j*)	**$DySc_2N$** (ref. 21*b*)	**$ErSc_2N$** (ref. 30)	
	2.149(10)	2.096(6)	2.089(9)	
M_2ScN	**Gd_2ScN** (ref. 10*j*)	**Dy_2ScN** (ref. 21*c*)		
	2.072(3)	2.078(6)		
	2.102(3)	*1.965(6) (overlap Sc)*[c]		
MM'_2N	**$DyGd_2N$**	**$DyGd_2N$**	**$DyEr_2N$**	**$CeLu_2N$** (ref. 12*b*)
	2.085(10)	2.034(10)	2.012(10)	2.016(7)
	2.097(11)	**$DyEr_2N$**	2.047(10)[d]	2.061(8)
		2.047(10)[d]	2.052(10)[d]	*2.038 (av)*[b]
		2.052(10)[d]		
DFT calculations				
	2.090 (Gd_3N)	2.063 (Dy_3N)	2.055 (Er_3N)	2.051 (Lu_3N)
	2.090 ($DyGd_2N$)	2.072 (Dy_2LaN)	2.049 ($DyEr_2N$)	2.036 ($DyLu_2N$)
	2.089 (Dy_2GdN)	2.063 (Dy_2GdN)	2.044 (Dy_2ErN)	2.020 (Dy_2LuN)
		2.064 (Dy_2YN)		
		2.064 (Dy_2ErN)		
		2.073 (Dy_2LuN)		
		2.106 (Dy_2ScN)		
		2.076 ($DyLa_2N$)		
		2.064 ($DyGd_2N$)		
		2.067 (DyY_2N)		
		2.070 ($DyEr_2N$)		
		2.090 ($DyLu_2N$)		
		2.156 ($DySc_2N$)		

[a] Shannon radii for the lanthanide 3+ ions in a six-coordinate environment from the study in ref. 22. [b] "av" stands for an averaged M–N bond length over two or three M–N bonds. [c] The bond length is strongly underestimated because of the disorder in the cluster and near overlap with the Sc site. [d] The value is likely to be an average of the Dy–N and Er–N bond lengths.

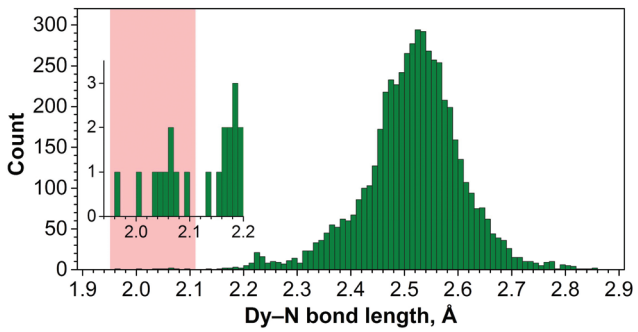

Fig. 8 Distribution of 5369 Dy–N bond lengths in molecular Dy compounds deposited in the Cambridge Structural Database. The range of Dy–N bond lengths in Dy-based $M_3N@C_{80}$ NCFs is highlighted in light red. The inset shows an expansion of the data in the short distance range; the abscissa scale for the inset and the main figure is the same.

length estimation unreliable. For the well-modeled Er1 atom in $DyEr_2N@C_{80}$, the Er1A–N bond is noticeably shorter than that in $Er_3N@C_{80}$, which indicates that the Dy–N bond can release its strain by elongation at the expense of the shortening of the Er–N bonds.

As a measure of the pyramidalization of the M_3N cluster it is convenient to use the displacement of the nitrogen atom from the metal plane (Table 2). For instance, in $Gd_3N@C_{80}$ and $Tb_3N@C_{80}$ nitrogen atoms are displaced above/below the M_3 plane by 0.522/0.463 and 0.453/0.405 Å, respectively (the nitrogen atom in these molecules is split between two sites, hence two different values).[3d,6a] In $DyGd_2N@C_{80}$ this displacement distance is 0.456/0.452 Å, somewhat smaller than that in Gd_3N but larger than that in the Tb_3N cluster. If the split-nitrogen model of the $Dy_3N@C_{80}$ data is adopted, the out-of-plane displacement of nitrogen in Dy_3N would be 0.26 Å (here the value is calculated as a half of the distance between two nitrogen sites). *I.e.*, pyramidalization is decreased considerably from Gd_3N over Tb_3N to Dy_3N.

For a deeper understanding of these phenomena, we also studied the pyramidalization of the nitride cluster in a series of lanthanide and mixed-lanthanide $M_3N@C_{80}$ molecules theoretically. DFT calculations were performed at the PBE-D level with a plane-wave basis set and corresponding projector augmented-wave potentials, treating 4f-electrons as a part of the core as implemented in the VASP 5.0 package.[36] The computed out-of-plane displacements of nitrogen for $Gd_3N@C_{80}$, $DyGd_2N@C_{80}$, and $Tb_3N@C_{80}$ are 0.468, 0.396, and 0.365 Å

Table 2 Pyramidalization of the nitride cluster in selected $M_3N@C_{80}$ NCFs measured as the out-of-plane displacement of the nitrogen atom, DFT-computed harmonic vibrational frequencies for the γ_{M_3N} mode and out-of-plane nitrogen displacement amplitude l_z at 100 K

$M_3N@C_{80}$-I_h[a]	X-ray, Å	DFT, Å	γ_{M_3N}, cm^{-1}	l_z[b], Å
$DyLa_2N@C_{80}$	—	0.820		
$Dy_2LaN@C_{80}$	—	0.593	159	0.096
$Gd_3N@C_{80}$	0.522(8)/0.463(14) (ref. 6*a*)	0.468	143	0.104
$DyGd_2N@C_{80}$	0.456(19)/0.452(12)	0.396		
$Tb_3N@C_{80}$	0.453(4)/0.405(7) (ref. 3*d*)	0.365	128	0.114
$CeLu_2N@C_{80}$	0.349(9)/0.324(9) (ref. 12*b*)	0.352	114	0.125
$Dy_2GdN@C_{80}$	—	0.311		
$Dy_3N@C_{80}$	0.068(11) (ref. 31)[c] 0.26 (ref. 6*b*)[d]	0.203	72	0.187
$Dy_2YN@C_{80}$	—	0.125	86	0.159
$DyY_2N@C_{80}$	—	0.087		
$Dy_2ErN@C_{80}$	—	0.086		
$Ho_3N@C_{80}$	0.058(9)[c] (ref. 6*b*) 0.090[d]	0.068	51	0.259
$Y_3N@C_{80}$	0.129(6) (ref. 38)[e]	0.059	74	0.183
$DyEr_2N@C_{80}$	0.050(11)	0.057		
$Dy_2LuN@C_{80}$	—	0.046		
$Er_3N@C_{80}$	0.025(3)[c] (ref. 6*b*) 0.064[d]	0.020	97	0.143
$Dy_2ScN@C_{80}$	0.116(8) (ref. 21*c*)	0.020	133	0.110
$DyLu_2N@C_{80}$	—	0.015	93	0.149
$DySc_2N@C_{80}$	0.003(12) (ref. 21*b*)	0.014	211	0.079
$Lu_3N@C_{80}$	0.0953(1) (ref. 34) 0.01(2) (ref. 35) 0.001(8) (ref. 3*c*)	0.007	145	0.103

[a] The molecules are listed in the descending order of their DFT-predicted pyramidalization (displacement of nitrogen from the metal plane). [b] l_z is computed as a square root of l^2 in eqn (1), in which ν and μ are substituted with the DFT vibrational frequency of the γ_{M_3N} mode and atomic mass of nitrogen, respectively. [c] Single nitrogen site. [d] Nitrogen is split between two sites and pyramidalization is computed as a half of the distance between two nitrogen sites. [e] In the pyrrolidine monoadduct.

respectively. Notably, for the midsize cluster in $Dy_3N@C_{80}$ calculations predict the value of 0.203 Å, but already in $DyEr_2N@C_{80}$ the cluster is nearly planar, with the nitrogen displacement amounting to only 0.057 Å (compare to the experimental result of 0.05(1) Å). Similarly, for $Dy_2GdN@C_{80}$ and $Dy_2ErN@C_{80}$ the calculation predicts a pyramidal cluster with a displacement parameter of 0.311 and 0.086 Å, respectively. Finally, nearly planar cluster geometries are also found for $Er_3N@C_{80}$ (0.020 Å) and $Lu_3N@C_{80}$ (0.007 Å). These computational results are in agreement with the trends predicted in other theoretical studies of $M_3N@C_{80}$ molecules.[13,37] Overall, DFT calculations support well the experimental observations of the strong cluster pyramidalization for Gd_3N and $DyGd_2N$, a moderately pyramidal cluster geometry in $Dy_3N@C_{80}$, and a nearly planar cluster in $DyEr_2N@C_{80}$. However, as we show below, a direct comparison of X-ray data and results of DFT calculations may be misleading if the real physical quantities behind diffraction data are not considered correctly.

Cluster pyramidalization and vibrational displacements

Structural analysis of NCFs such as that given in the previous section or in numerous publications on this subject (see ref. 6*b* for a systematic analysis of $M_3N@C_{80}$ structures) implicitly assumes that X-ray diffraction provides the ground state geometry of the molecule. Strictly speaking, this is not entirely correct. Thermal motion of atoms and population of excited vibrational levels may significantly distort the observed structure, especially if the potential energy surface is rather shallow. Since these effects may affect the interpretation of the diffraction data substantially, we decided to analyze in depth how vibrational degrees of freedom may influence the structure of the nitride cluster.

Harmonic approximation

DFT-based vibrational analysis of $M_3N@C_{80}$ NCF molecules (M = Y, Gd–Er, Table 2) shows that vibrations of the nitrogen atom in these molecules are well separated from vibrational displacements of the other atoms. Three degrees of freedom of the nitrogen atom produce two vibrational modes of the M_3N cluster. The displacement of the nitrogen perpendicular to the plane of metals forms the cluster deformation mode (γ_{M_3N}), whereas the in-plane motion constitutes the two-fold degenerate antisymmetric M–N stretching mode (ν_{asM-N}). The ν_{asM-N} mode occurs at frequencies of 700–750 cm^{-1} and is easily detectable in IR spectra due to its medium-strong intensity.[31,39] The out-of-plane oscillation frequency predicted in the harmonic approximation depends strongly on the metal size and ranges from 256 cm^{-1} in $Sc_3N@C_{80}$ (exp. value is 236 cm^{-1}, ref. 40) over 145 cm^{-1} in $Lu_3N@C_{80}$ and down to 51 cm^{-1} in $Ho_3N@C_{80}$, for which DFT predicts the lowest γ_{M_3N} frequency in the whole $M_3N@C_{80}$ series (Table 2). The fre-

quency variation from Sc to Lu and Ho reflects the trend of the M_3N cluster to flatten its potential energy surface along the pyramidalization coordinate with the increase of the metal size. When the metal size increases beyond Ho, the cluster adopts a pyramidal shape with a double-well energy potential, and the calculated γ_{M_3N} frequency increases again from 72 cm^{-1} in $Dy_3N@C_{80}$ to 128 cm^{-1} in $Tb_3N@C_{80}$ and 143 cm^{-1} in $Gd_3N@C_{80}$.

The large difference of the γ_{M_3N} and ν_{asM-N} vibrational frequencies results in a more pronounced out-of-plane displacement of the nitrogen atom in $M_3N@C_{80}$, leading to an elongation of the nitrogen thermal ellipsoid in the out-of-plane direction. In the harmonic approximation, which implies that the energy is a quadratic function of atomic displacements, the thermal displacements can be calculated as the root-mean-square vibrational amplitudes of a quantum harmonic oscillator:[41]

$$\langle l^2 \rangle = \left(\frac{h}{8\pi^2 \mu \nu} cth\left\{ \frac{h\nu}{2k_B T} \right\} \right) \quad (1)$$

where μ is a reduced mass, and ν is a vibrational frequency. Since in-plane and out-of-plane oscillations of nitrogen in $M_3N@C_{80}$ are well separated, we can compute the out-of-plane (l_z) and in-plane ($l_{x,y}$) nitrogen amplitudes as a square root of $\langle l^2 \rangle$ in eqn (1), in which μ is substituted by the atomic mass of nitrogen, and ν is either the vibrational frequency of the γ_{M_3N} mode (giving l_z) or the frequency of the ν_{asM-N} mode (giving $l_{x,y}$). At a temperature of 100 K often used in XRD studies of fullerene crystals, the calculated out-of-plane and in-plane nitrogen amplitudes are $l_z/l_{x,y}$ = 0.074/0.045 Å in $Sc_3N@C_{80}$, 0.103/0.041 Å in $Lu_3N@C_{80}$, 0.259/0.040 Å in $Ho_3N@C_{80}$, and 0.187/0.040 Å in $Dy_3N@C_{80}$. Even at 0 K, zero-point motion for the oscillator with a frequency of 80 cm^{-1} has an amplitude of 0.123 Å, and with the increase of temperature to 100 K the amplitude may reach 0.170 Å due to the population of vibrational excited states (for ν = 80 cm^{-1}, the populations of the first three levels at 100 K are 0.68, 0.22, and 0.07). One should also note that in the excited states the probability density moves closer to the edges of the potential well, as opposed to the center of the well for the zeroth level, which increases the probability to find the nitrogen atom above and below the metal plane even if the cluster has a planar geometry in the ground state.

To summarize, rather large vibrational displacements of the nitrogen atom may potentially lead to erroneous conclusions on the perceived cluster geometry. When the cluster is on the edge between planar and pyramidal shapes, the potential energy surface is flat, and the vibrational frequency of the out-of-plane deformation is low. This defines the large vibrational amplitudes of *ca.* 0.2 Å and partial localization of the probability density above and below the metal plane. The thermal ellipsoid of nitrogen should then be strongly elongated, and the question whether nitrogen should be treated as a single site ("planar cluster") or split into two sites ("pyramidal cluster") may become very ambiguous.

Beyond harmonic approximation

Simple harmonic approximation already points to the potentially complicated contribution of vibrational motion to the experimental molecular structure. But flat energy potentials and large vibrational amplitudes also indicate that the harmonic approximation may not be adequate by itself. A more reliable description of the system requires explicit consideration of the energy potential along the pyramidalization coordinate. With the use of DFT, we obtained potentials for five $M_3N@C_{80}$ molecules by optimizing their structures with the nitrogen atom fixed at different distances above and below the plane of metal atoms (Fig. 9).

For the strongly pyramidal Gd_3N cluster in $Gd_3N@C_{80}$, the energy profile ($E(z)$) has a classical double-well potential shape with the minima for the nitrogen atom at 0.45 Å above and below the Gd_3 plane (Fig. 10). Quite common in many fields of

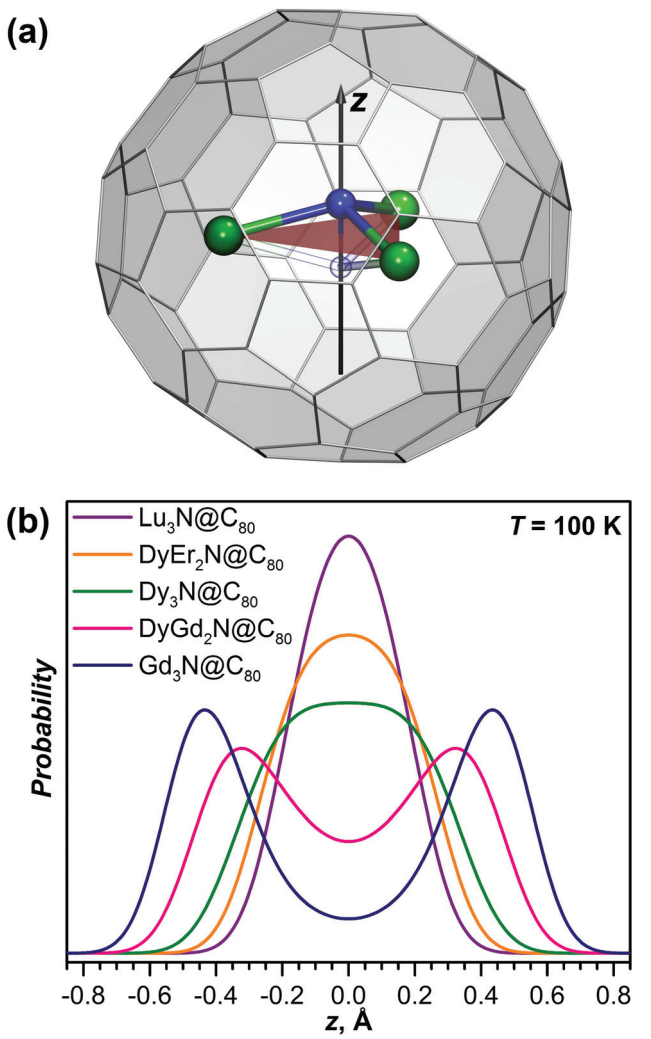

Fig. 9 (a) Molecular structure of $M_3N@C_{80}$ with a pyramidal cluster and definition of the axis z used in the analysis; an equivalent position of the nitrogen atom below the plane of metal atoms is semitransparent. (b) Probability density for finding the nitrogen atom at a certain position along the z axis in different $M_3N@C_{80}$ molecules computed for T = 100 K as the temperature often used in X-ray diffraction studies of EMFs.

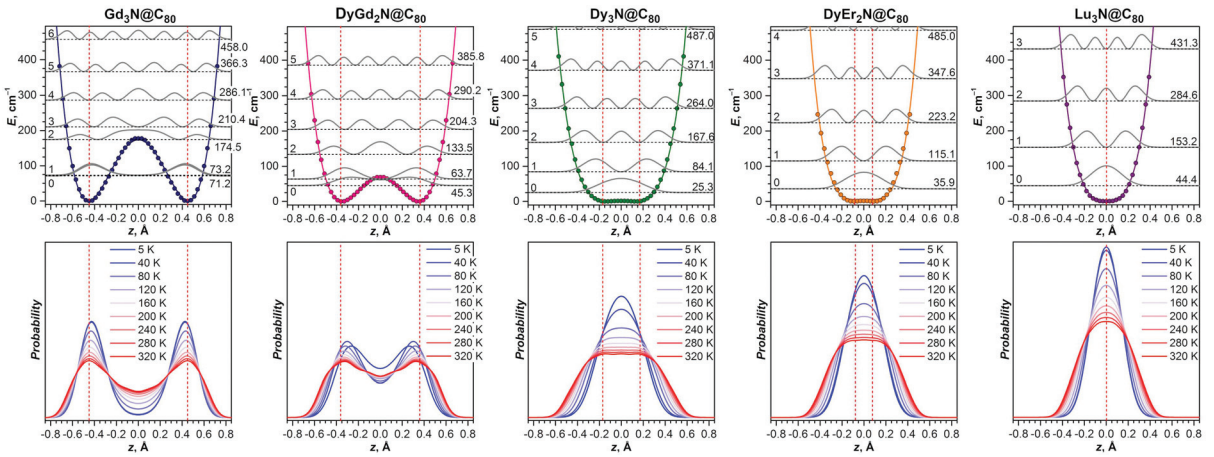

Fig. 10 Potential energy profiles (top row) and probability densities at different temperatures (bottom row) for the pyramidalization of the M_3N cluster in $M_3N@C_{80}$ molecules with different cluster compositions and sizes. In potential energy profiles dots are results of DFT calculations, solid colored lines are fits of DFT results with the $Az^4 - Bz^2$ function, red dashed vertical lines mark positions of the minima of the potential, dashed horizontal lines are vibrational levels obtained by the solution of the Schrödinger equation and gray solid lines are probability densities for each vibrational level (*i.e.* $|\Psi_n^2|$ function for the *n*th level). For the sake of comparison probability densities for different $M_3N@C_{80}$ molecules in the bottom row are shown on one scale.

analytical physics, the double-well potentials are well developed and understood since the studies of pyramidal inversion in NH_3 and related molecules.[42] The $E(z)$ maximum at $z = 0$ Å, *i.e.* the pyramidal inversion barrier, is only 177 cm^{-1} in $Gd_3N@C_{80}$. The symmetrized *ab initio* potential profile (dots in Fig. 10) can be described well using an analytical function $E(z) = Az^4 - Bz^2$ (solid lines in Fig. 10). After fitting A and B parameters the Schrödinger equation is solved numerically using this analytical potential and a particle mass equal to that of a nitrogen atom (14 Da), which gives a quasi-degenerate ground state for $Gd_3N@C_{80}$ with the symmetric and antisymmetric state energies of 71.2 and 73.2 cm^{-1}, respectively, and an inversion splitting of 2 cm^{-1}. The probability to find the nitrogen atom at a certain z-position (defined as a square of the wavefunction $|\Psi_n^2|$ for the nth state) has two maxima closely coinciding with the potential minima. Thus, the pyramidal shape of the Gd_3N cluster is well defined since the zeroth ($|0\rangle$) and first ($|1\rangle$) vibrational levels lie within the potential wells. However, already the second energy level at 174.5 cm^{-1} almost coincides with the inversion barrier, and $|\Psi_2^2|$ has a broad maximum at $z = 0$. At higher energy, the structure of the vibrational levels resembles that of a system with a harmonic potential, although the levels are not equidistant.

The experimentally observable positions of the nitrogen (*e.g.*, from diffraction data) correspond to the maxima of the total probability density, which is temperature dependent because of the variation of thermal populations of the energy levels. The probability density at a temperature T can be obtained as a sum $\sum_n p_n(T)|\Psi_n^2|$, where $p_n(T)$ are weight factors determined from Boltzmann distribution, $p_n(T) \sim \exp(-\varepsilon_n/k_BT)\left(\sum_i \exp(-\varepsilon_i/k_BT)\right)^{-1}$. For $Gd_3N@C_{80}$ we find a well-behaving double maximum picture (Fig. 9b and 10) with a slight temperature variation of the maximum position and a considerable broadening of the distribution. Yet two maxima are clearly seen up to room temperature ensuring that X-ray diffraction data give a correct description of the pyramidal Gd_3N cluster.

A double-well energy profile with an inversion barrier of only 69 cm^{-1} is found for $DyGd_2N@C_{80}$. The decrease of the barrier caused by the reduced size of the M_3N cluster leads to a considerable change in the structure of the vibrational levels in comparison with those in $Gd_3N@C_{80}$. The ground vibrational level of $DyGd_2N@C_{80}$ is found at 45.3 cm^{-1}, which lies within the double-well. However, the $|\Psi_0^2|$ function has a complex shape with two broad and strongly overlapping peaks, whose maxima are shifted from the positions of the potential minima to much smaller z values. Thus, if X-ray diffraction would be performed at helium temperature, an apparent pyramidalization deduced from diffraction data would be underestimated or even missed because the probability minimum at $z = 0$ is rather shallow. The first excited vibrational level of $DyGd_2N@C_{80}$ is located at 63.7 cm^{-1}. Note that the quasi-degeneracy of the $|0\rangle$ and $|1\rangle$ levels observed in $Gd_3N@C_{80}$ is lifted here. The $|\Psi_1^2|$ distribution has a more common shape with two well-defined maxima near the positions corresponding to the minima of the energy profile. Considerable alteration of the shape of the $|\Psi_0^2|$ and $|\Psi_1^2|$ functions and a comparably small energy difference between the levels lead to pronounced changes in the probability density even after a modest temperature increase from 5 to 40 K: the maxima become sharper and shift further away from each other, whereas the minimum between them becomes more pronounced. Thus, the temperature increase will result in rather counterintuitive changes in the diffraction data as positions of nitrogen will be better defined at a higher temperature than

near 0 K. The second and higher excited vibrational levels of $DyGd_2N@C_{80}$ resemble the levels of a system with a single energy minimum. A temperature increase above 40 K leads to a gradual shift of the probability maxima to higher $|z|$ values and broadening of the probability density.

The decrease of the cluster size to that of Dy_3N results in a conceptual change of the form of the potential energy profile. Although its double-well nature with the minima near $|z|$ = 0.2 Å is formally preserved, the inversion barrier is reduced to a small value of 1.5 cm^{-1}, which is already comparable to the numerical precision of the computational approach. The ground vibrational level is found at 25.3 cm^{-1}, considerably higher than the inversion barrier, and $|\Psi_0^2|$ has a single maximum at z = 0. Essentially the structure of vibrational levels in $Dy_3N@C_{80}$ is that of a system with a single well potential. Substantial anharmonicity of the potential, which has $\sim z^4$ dependence, leads to a non-equidistant spacing of the levels. The probability density for the nitrogen position in $Dy_3N@C_{80}$ has a single-peak shape at all temperatures. The peak is rather broad and gets flattened at higher temperatures. Thus, one can expect that the diffraction data for Dy_3N should show a single nitrogen position with an anomalously elongated thermal ellipsoid as was indeed reported in ref. 31.

A situation similar to Dy_3N is also predicted for the $DyEr_2N$ and Lu_3N clusters. The pyramidalization of the cluster and inversion barrier in $DyEr_2N$ are even smaller than those in Dy_3N. In $Lu_3N@C_{80}$, a single energy minimum is found. The potential is not harmonic even for the relatively small Lu_3N cluster and for both molecules it is well described by a quartic function with only a small contribution of z^2. A decrease of the cluster size results in a narrowing of the potential well and an increase of the distance between vibrational levels. Accordingly, the probability density with the maximum at z = 0 becomes narrower with the decrease of the cluster size. Thus, diffraction data should give a planar structure of the M_3N cluster with a gradual decrease of the elongation of the nitrogen ellipsoid from Dy_3N over $DyEr_2N$ to Lu_3N.

Fig. 11 compares probability densities, obtained from computational studies of $DyGd_2N@C_{80}$ and $DyEr_2N@C_{80}$, to the difference in the electron density near the position of the nitrogen, obtained by subtracting the density reconstructed from the refined positions of all atoms except nitrogen from the experimental density determined by X-ray diffraction. Good agreement between experiment and theory can be observed. For $DyGd_2N@C_{80}$, an elongated density profile with two well-defined maxima can be distinguished and the maxima are close to the maxima in the probability density function. For $DyEr_2N@C_{80}$, a single density lobe is seen and its spatial extension along the z-axis corresponds to the peak shape of the probability density.

To summarize, the analysis of the potential energy profile along the cluster pyramidalization coordinate shows that precise structure determination of the M_3N cluster from diffraction data may be complicated. Calculations show a gradual development of the double-well potential with increasing metal size, which means that the pyramidalization of the M_3N cluster should increase gradually as long as the metal size is larger than that of Lu. However, if the inversion barrier is below the lowest vibrational level, the probability density has a single maximum (Fig. 9b and 10). Diffraction methods (which do not restore the shape of the potential but determine high-probability atomic positions) should then give the planar shape of the cluster even when the energy profile has two minima. At the same time, the thermal ellipsoid of nitrogen should be strongly elongated in the direction perpendicular to the metal plane. Description with single or split nitrogen positions may then give similar R-factors. A true pyramidal shape of the cluster can be obtained when at least one vibrational level of the system lies below the inversion barrier. But even in this case, a mismatch between the shape of the potential and probability density function, *i.e.* when the maxima in the latter do not correspond to the minima in the former, can be rather strong, as found here for the $DyGd_2N$ cluster, and pyramidalization deduced from diffraction data should exhibit considerable temperature dependence. Only when two or more vibrational levels are below the inversion barrier, as found for $Gd_3N@C_{80}$, a stable pyramidal shape of the cluster with moderate temperature dependence can be observed by X-ray diffraction. Needless to say, additional disorder of the fullerene cage and metal positions will further complicate the situation. Thus, the molecular structure elucidation of endohedral fullerenes with labile endohedral species at a single temperature may give ambiguous results. Variable temperature studies with

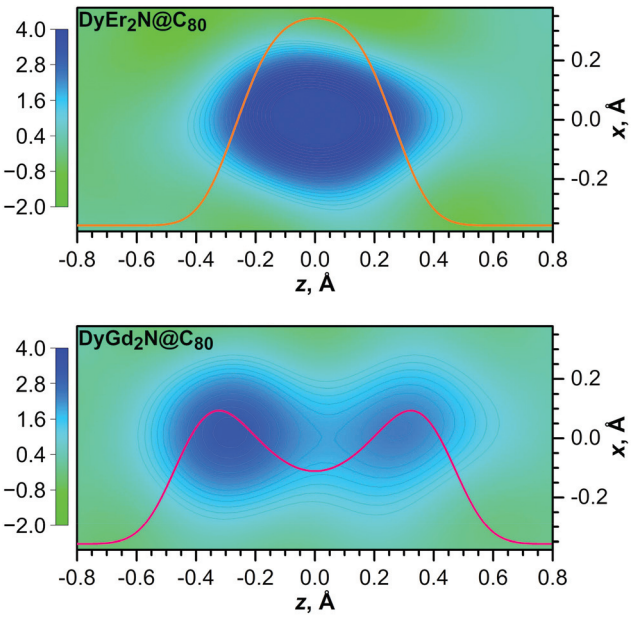

Fig. 11 Difference electron density maps for the nitrogen atom in $DyEr_2N@C_{80}$ (top) and $DyGd_2N@C_{80}$ (bottom). The calculated density was built using refined positions and structure factors of all atoms except nitrogen. 2D maps of the density are overlaid with the probability density function for the nitrogen atom at the z-coordinate computed for 100 K (the same as in Fig. 9). For the sake of comparison the color scale and the scale for probability density are the same for both molecules.

careful analysis of thermal motion are needed to address this problem.[43]

In the end we would like to note that parameters of the double-well potentials found in this work for $M_3N@C_{80}$ molecules with large endohedral clusters may be of use for design of the sources of terahertz radiation or even masers. The very first two-state maser system designed back in 1954 [44] utilized ammonia gas and operated at a frequency of 24.0 GHz corresponding to an inversion splitting of 0.8 cm^{-1} in an NH_3 molecule. The inversion barrier of 177 cm^{-1} in $Gd_3N@C_{80}$ is almost an order of magnitude smaller than the insertion barrier of 2020 cm^{-1} in NH_3, but the vibration effective mass of 14 Da is an order of magnitude greater in $Gd_3N@C_{80}$ against 1 Da for ammonia. Thus, the transmission coefficient for the quantum tunneling defined as $\exp\left(-2\int_{\Delta z} dz\sqrt{2m_{\text{eff}}|E(z)-\varepsilon|}\right)$ in the Wentzel–Kramers–Brillouin approximation is of the same order for both molecules and hence similar quantum dynamics can be expected for them. Without going into deep detail at this moment, we just highlight that the $Gd_3N@C_{80}$ system may be driven and modulated by an external electric field in the same way and fashion as is possible for the ammonia system and hence $Gd_3N@C_{80}$ is a prospective candidate for a two-state maser system with an operating frequency of 60.0 GHz (inversion splitting: 2 cm^{-1}). A combination of other lanthanides can be used to tune the shape of the double-well potential and hence the inversion splitting and operating frequency. Differently from the ammonia gas, in the case of the fullerene crystal the M_3N units are encapsulated in carbon cages and hence are well-separated from each other and isolated from the environment. Thus, the M_3N-based maser combines the simplicity of the ammonia maser (two-state system; no need for pumping as the energy split is small; a lack of spontaneous emission) with higher efficiency in amplification and higher photon densities due to the solid state density of the M_3N units in the crystal.[45]

Conclusions

In this work we have undertaken a systematic exploration of various Dy-lanthanide combinations in the synthesis of mixed-metal nitride clusterfullerenes. A variation of the size of the metal combined with Dy offered a possibility to gradually tune the size of the nitride cluster and study the influence of this factor on the synthesis and structure. The ionic radius of the metal employed in the synthesis is shown to be the main factor affecting the relative yield of the majority of $Dy_xM_{3-x}N@C_{80}$ species. Yet, the electronic properties of metals such as the third ionization potential, also play an important role and may cause completely unexpected distribution of products, such as that demonstrated in this work for the Dy–Tm system.

A single-crystal X-ray diffraction study of the molecular structures of $DyGd_2N@C_{80}$ and $DyEr_2N@C_{80}$ along with DFT computation for a broad range of $Dy_xM_{3-x}N@C_{80}$ molecules offered a possibility to analyze how the variation of the size of the nitride cluster affects its shape. DFT calculations showed that a gradual increase of the metal size leads to the variation of the cluster shape from a planar triangle when the cluster is relatively small to a trigonal pyramid with gradually increasing height when the metal size increases. For pyramidal clusters the energy profile along the pyramidalization coordinate has a double-well shape. At the same time, calculations show that the inversion barrier for the pyramidal inversion in the M_3N cluster is quite small. This situation results in a fundamental problem for structure determination rooted in the quantum nature of molecular vibrations: if the energy of the zeroth vibrational level is higher than the inversion barrier, the apparent structure of the pyramidal M_3N cluster as perceived from diffraction data will be planar. Particularly interesting is the situation when the inversion barrier is comparable to the lowest-energy vibrational levels. In this case, quantum effects may reveal themselves as the strong variation of the probability distribution with temperature and potentially may be detected by variable-temperature X-ray diffraction experiments or spectroscopic studies. Finally, we propose that the double-well potential and inversion splitting of the levels for larger M_3N clusters have a number of parameters which make them prospective candidates for terahertz light applications.

Conflicts of interest

There are no conflicts to declare.

Acknowledgements

The authors acknowledge funding from the European Union's Horizon 2020 research and innovation programme, European Research Council (grant agreement No 648295 to A. A. P.) and Marie Skłodowska-Curie action (grant agreement No. 748635 to S. M. A.) and the Deutsche Forschungsgemeinschaft (grants PO 1602/4-1 and PO 1602/5-1 to A. A. P.). Diffraction data have been collected on BL14.3 at the BESSY II electron storage ring operated by the Helmholtz-Zentrum Berlin; we would particularly like to acknowledge the help and support of Manfred Weiss and his group members during the experiments at BESSY II. Computational resources were provided by the Center for High Performance Computing at the TU Dresden. We appreciate the technical support with computational resources in IFW Dresden by Ulrike Nitzsche. Sandra Schiemenz is acknowledged for the help with spectroscopic measurements.

References

1 (*a*) J. Zhang, S. Stevenson and H. C. Dorn, *Acc. Chem. Res.*, 2013, **46**, 1548; (*b*) L. Dunsch and S. Yang, *Small*, 2007, **3**, 1298; (*c*) M. N. Chaur, F. Melin, A. L. Ortiz and L. Echegoyen, *Angew. Chem., Int. Ed.*, 2009, **48**, 7514; (*d*) A. A. Popov, S. Yang and L. Dunsch, *Chem. Rev.*, 2013,

113, 5989; (*e*) S. Yang, T. Wei and F. Jin, *Chem. Soc. Rev.*, 2017, **46**, 5005.

2 S. Stevenson, G. Rice, T. Glass, K. Harich, F. Cromer, M. R. Jordan, J. Craft, E. Hadju, R. Bible, M. M. Olmstead, K. Maitra, A. J. Fisher, *et al.*, *Nature*, 1999, **401**, 55.

3 (*a*) S. F. Yang and L. Dunsch, *J. Phys. Chem. B*, 2005, **109**, 12320; (*b*) M. Krause, J. Wong and L. Dunsch, *Chem. – Eur. J.*, 2005, **11**, 706; (*c*) W. Shen, L. B. Bao, S. Hu, X. Gao, Y. Xie, X. Gao, W. Huang and X. Lu, *Chem. – Eur. J.*, 2018, **24**, 16692; (*d*) T. M. Zuo, C. M. Beavers, J. C. Duchamp, A. Campbell, H. C. Dorn, M. M. Olmstead and A. L. Balch, *J. Am. Chem. Soc.*, 2007, **129**, 2035; (*e*) L. Dunsch, M. Krause, J. Noack and P. Georgi, *J. Phys. Chem. Solids*, 2004, **65**, 309; (*f*) W. Fu, L. Xu, H. Azurmendi, J. Ge, T. Fuhrer, T. Zuo, J. Reid, C. Shu, K. Harich and H. C. Dorn, *J. Am. Chem. Soc.*, 2009, **131**, 11762; (*g*) M. N. Chaur, A. J. Athans and L. Echegoyen, *Tetrahedron*, 2008, **64**, 11387.

4 (*a*) A. A. Popov and L. Dunsch, *J. Am. Chem. Soc.*, 2007, **129**, 11835; (*b*) A. Rodriguez-Fortea, N. Alegret, A. L. Balch and J. M. Poblet, *Nat. Chem.*, 2010, **2**, 955; (*c*) K. Nakao, N. Kurita and M. Fujita, *Phys. Rev. B: Condens. Matter Mater. Phys.*, 1994, **49**, 11415.

5 (*a*) F. Melin, M. N. Chaur, S. Engmann, B. Elliott, A. Kumbhar, A. J. Athans and L. Echegoyen, *Angew. Chem., Int. Ed.*, 2007, **46**, 9032; (*b*) M. N. Chaur, F. Melin, B. Elliott, A. Kumbhar, A. J. Athans and L. Echegoyen, *Chem. – Eur. J.*, 2008, **14**, 4594; (*c*) M. N. Chaur, F. Melin, J. Ashby, A. Kumbhar, A. M. Rao and L. Echegoyen, *Chem. – Eur. J.*, 2008, **14**, 8213.

6 (*a*) S. Stevenson, J. P. Phillips, J. E. Reid, M. M. Olmstead, S. P. Rath and A. L. Balch, *Chem. Commun.*, 2004, 2814; (*b*) M. M. Olmstead, T. Zuo, H. C. Dorn, T. Li and A. L. Balch, *Inorg. Chim. Acta*, 2017, **468**, 321.

7 N. Chen, L. Z. Fan, K. Tan, Y. Q. Wu, C. Y. Shu, X. Lu and C. R. Wang, *J. Phys. Chem. C*, 2007, **111**, 11823.

8 S. Yang, C. Chen, A. Popov, W. Zhang, F. Liu and L. Dunsch, *Chem. Commun.*, 2009, 6391.

9 T. Wei, S. Wang, X. Lu, Y. Tan, J. Huang, F. Liu, Q. Li, S. Xie and S. Yang, *J. Am. Chem. Soc.*, 2016, **138**, 207.

10 (*a*) N. Chen, E. Y. Zhang and C. R. Wang, *J. Phys. Chem. B*, 2006, **110**, 13322; (*b*) Y. Zhang, K. B. Ghiassi, Q. Deng, N. A. Samoylova, M. M. Olmstead, A. L. Balch and A. A. Popov, *Angew. Chem., Int. Ed.*, 2015, **52**, 495; (*c*) S. Stevenson, C. B. Rose, J. S. Maslenikova, J. R. Villarreal, M. A. Mackey, B. Q. Mercado, K. Chen, M. M. Olmstead and A. L. Balch, *Inorg. Chem.*, 2012, **51**, 13096; (*d*) X. L. Wang, T. M. Zuo, M. M. Olmstead, J. C. Duchamp, T. E. Glass, F. Cromer, A. L. Balch and H. C. Dorn, *J. Am. Chem. Soc.*, 2006, **128**, 8884; (*e*) Y. Zhang, A. A. Popov and L. Dunsch, *Nanoscale*, 2014, **6**, 1038; (*f*) Y. Zhang, S. Schiemenz, A. A. Popov and L. Dunsch, *J. Phys. Chem. Lett.*, 2013, **4**, 2404; (*g*) S. Yang, A. A. Popov, C. Chen and L. Dunsch, *J. Phys. Chem. C*, 2009, **113**, 7616; (*h*) A. L. Svitova, A. A. Popov and L. Dunsch, *Inorg. Chem.*, 2013, **52**, 3368; (*i*) Y. Zhang, D. Krylov, M. Rosenkranz, S. Schiemenz and A. A. Popov, *Chem. Sci.*, 2015, **6**, 2328; (*j*) S. Stevenson, C. Chancellor, H. M. Lee, M. M. Olmstead and A. L. Balch, *Inorg. Chem.*, 2008, **47**, 1420; (*k*) Y. Zhang, A. A. Popov, S. Schiemenz and L. Dunsch, *Chem. – Eur. J.*, 2012, **18**, 9691; (*l*) R. M. Macfarlane, D. S. Bethune, S. Stevenson and H. C. Dorn, *Chem. Phys. Lett.*, 2001, **343**, 229; (*m*) M. Nie, J. Xiong, C. Zhao, H. Meng, K. Zhang, Y. Han, J. Li, B. Wang, L. Feng, C. Wang and T. Wang, *Nano Res.*, 2019, **12**, 1727.

11 C. Chen, F. Liu, S. Li, N. Wang, A. A. Popov, M. Jiao, T. Wei, Q. Li, L. Dunsch and S. Yang, *Inorg. Chem.*, 2012, **51**, 3039.

12 (*a*) L. Zhang, A. A. Popov, S. Yang, S. Klod, P. Rapta and L. Dunsch, *Phys. Chem. Chem. Phys.*, 2010, **12**, 7840; (*b*) S. Stevenson, H. R. Thompson, K. D. Arvola, K. B. Ghiassi, M. M. Olmstead and A. L. Balch, *Chem. – Eur. J.*, 2015, **21**, 10362.

13 Z. Zhang, Y. Liu, P. Han, S. Zhuang, T. Wang, S. Luo and B. Xu, *ChemPhysChem*, 2015, **16**, 295.

14 E. B. Iezzi, J. C. Duchamp, K. R. Fletcher, T. E. Glass and H. C. Dorn, *Nano Lett.*, 2002, **2**, 1187.

15 Y. Zhang, D. Krylov, S. Schiemenz, M. Rosenkranz, R. Westerstrom, J. Dreiser, T. Greber, B. Buchner and A. A. Popov, *Nanoscale*, 2014, **6**, 11431.

16 S. Yang, A. A. Popov and L. Dunsch, *Angew. Chem., Int. Ed.*, 2008, **47**, 8196.

17 N. Chen, E. Y. Zhang, K. Tan, C. R. Wang and X. Lu, *Org. Lett.*, 2007, **9**, 2011.

18 (*a*) R. Westerström, J. Dreiser, C. Piamonteze, M. Muntwiler, S. Weyeneth, K. Krämer, S.-X. Liu, S. Decurtins, A. Popov, S. Yang, L. Dunsch and T. Greber, *Phys. Rev. B: Condens. Matter Mater. Phys.*, 2014, **89**, 060406; (*b*) A. L. Svitova, Y. Krupskaya, N. Samoylova, R. Kraus, J. Geck, L. Dunsch and A. A. Popov, *Dalton Trans.*, 2014, **43**, 7387; (*c*) L. Spree and A. A. Popov, *Dalton Trans.*, 2019, **48**, 2861.

19 A. A. Popov and L. Dunsch, *Chem. – Eur. J.*, 2009, **15**, 9707.

20 (*a*) V. Vieru, L. Ungur and L. F. Chibotaru, *J. Phys. Chem. Lett.*, 2013, **4**, 3565; (*b*) F. Cimpoesu, N. Dragoe, H. Ramanantoanina, W. Urland and C. Daul, *Phys. Chem. Chem. Phys.*, 2014, **16**, 11337; (*c*) C.-H. Chen, D. S. Krylov, S. M. Avdoshenko, F. Liu, L. Spree, R. Yadav, A. Alvertis, L. Hozoi, K. Nenkov, A. Kostanyan, T. Greber, A. U. B. Wolter, *et al.*, *Chem. Sci.*, 2017, **8**, 6451.

21 (*a*) R. Westerström, J. Dreiser, C. Piamonteze, M. Muntwiler, S. Weyeneth, H. Brune, S. Rusponi, F. Nolting, A. Popov, S. Yang, L. Dunsch and T. Greber, *J. Am. Chem. Soc.*, 2012, **134**, 9840; (*b*) D. Krylov, F. Liu, A. Brandenburg, L. Spree, V. Bon, S. Kaskel, A. Wolter, B. Buchner, S. Avdoshenko and A. A. Popov, *Phys. Chem. Chem. Phys.*, 2018, **20**, 11656; (*c*) D. S. Krylov, F. Liu, S. M. Avdoshenko, L. Spree, B. Weise, A. Waske, A. U. B. Wolter, B. Büchner and A. A. Popov, *Chem. Commun.*, 2017, **53**, 7901.

22 R. Shannon, *Acta Crystallogr., Sect. A: Cryst. Phys., Diffr., Theor. Gen. Crystallogr.*, 1976, **32**, 751.

23 S. F. Yang, M. Kalbac, A. Popov and L. Dunsch, *ChemPhysChem*, 2006, **7**, 1990.
24 T. Okazaki, K. Suenaga, Y. F. Lian, Z. N. Gu and H. Shinohara, *J. Mol. Graphics*, 2001, **19**, 244.
25 M. Krause, X. J. Liu, J. Wong, T. Pichler, M. Knupfer and L. Dunsch, *J. Phys. Chem. A*, 2005, **109**, 7088.
26 (*a*) A. A. Popov and L. Dunsch, *J. Am. Chem. Soc.*, 2008, **130**, 17726; (*b*) R. Valencia, A. Rodriguez-Fortea, A. Clotet, C. de Graaf, M. N. Chaur, L. Echegoyen and J. M. Poblet, *Chem. – Eur. J.*, 2009, **15**, 10997.
27 (*a*) K. M. Sparta, M. Krug, U. Heinemann, U. Mueller and M. S. Weiss, *J. Appl. Crystallogr.*, 2016, **49**, 1085; (*b*) U. Mueller, R. Förster, M. Hellmig, F. U. Huschmann, A. Kastner, P. Malecki, S. Pühringer, M. Röwer, K. Sparta, M. Steffien, M. Ühlein, P. Wilk, *et al.*, *Eur. Phys. J. Plus*, 2015, **130**, 141.
28 V. Dubrovin, L.-H. Gan, B. Büchner, A. A. Popov and S. M. Avdoshenko, *Phys. Chem. Chem. Phys.*, 2019, **21**, 8197.
29 (*a*) H. Yang, C. M. Beavers, Z. Wang, A. Jiang, Z. Liu, H. Jin, B. Q. Mercado, M. M. Olmstead and A. L. Balch, *Angew. Chem., Int. Ed.*, 2010, **49**, 886; (*b*) H. Yang, Z. Wang, H. Jin, B. Hong, Z. Liu, C. M. Beavers, M. M. Olmstead and A. L. Balch, *Inorg. Chem.*, 2013, **52**, 1275; (*c*) H. Yang, H. Jin, X. Wang, Z. Liu, M. Yu, F. Zhao, B. Q. Mercado, M. M. Olmstead and A. L. Balch, *J. Am. Chem. Soc.*, 2012, **134**, 14127.
30 M. M. Olmstead, A. de Bettencourt-Dias, J. C. Duchamp, S. Stevenson, H. C. Dorn and A. L. Balch, *J. Am. Chem. Soc.*, 2000, **122**, 12220.
31 S. F. Yang, S. I. Troyanov, A. A. Popov, M. Krause and L. Dunsch, *J. Am. Chem. Soc.*, 2006, **128**, 16733.
32 (*a*) J. Zhang, W. Yi, Z. Chen and X. Zhou, *Dalton Trans.*, 2013, **42**, 5826; (*b*) S. Anfang, K. Harms, F. Weller, O. Borgmeier, H. Lueken, H. Schilder and K. Dehnicke, *Z. Anorg. Allg. Chem.*, 1998, **624**, 159; (*c*) K. L. M. Harriman, J. L. Brosmer, L. Ungur, P. L. Diaconescu and M. Murugesu, *J. Am. Chem. Soc.*, 2017, **139**, 1420; (*d*) L. Zhao, S. Xue and J. Tang, *Inorg. Chem.*, 2012, **51**, 5994; (*e*) P. Zhang, L. Zhang, C. Wang, S. Xue, S.-Y. Lin and J. Tang, *J. Am. Chem. Soc.*, 2014, **136**, 4484.
33 A. G. Orpen, L. Brammer, F. H. Allen, O. Kennard, D. G. Watson and R. Taylor, *J. Chem. Soc., Dalton Trans.*, 1989, S81–S83.
34 S. Stevenson, H. M. Lee, M. M. Olmstead, C. Kozikowski, P. Stevenson and A. L. Balch, *Chem. – Eur. J.*, 2002, **8**, 4528.
35 A. Voevodin, L. Abella, E. Castro, D. W. Paley, L. M. Campos, A. Rodríguez-Fortea, J. M. Poblet, L. Echegoyen and X. Roy, *Chem. – Eur. J.*, 2017, **23**, 13305.
36 (*a*) J. Hafner, *J. Comput. Chem.*, 2008, **29**, 2044; (*b*) G. Kresse and J. Hafner, *Phys. Rev. B: Condens. Matter Mater. Phys.*, 1993, **47**, 558; (*c*) G. Kresse and D. Joubert, *Phys. Rev. B: Condens. Matter Mater. Phys.*, 1999, **59**, 1758; (*d*) J. P. Perdew, K. Burke and M. Ernzerhof, *Phys. Rev. Lett.*, 1996, **77**, 3865; (*e*) S. Grimme, *Wiley Interdiscip. Rev.: Comput. Mol. Sci.*, 2011, **1**, 211.
37 X. Aparicio-Anglès, N. Alegret, A. Clotet, A. Rodríguez-Fortea and J. M. Poblet, *J. Phys. Chem. C*, 2013, **117**, 12916.
38 L. Echegoyen, C. J. Chancellor, C. M. Cardona, B. Elliott, J. Rivera, M. M. Olmstead and A. L. Balch, *Chem. Commun.*, 2006, 2653.
39 A. A. Popov, *J. Comput. Theor. Nanosci.*, 2009, **6**, 292.
40 M. Krause, H. Kuzmany, P. Georgi, L. Dunsch, K. Vietze and G. Seifert, *J. Chem. Phys.*, 2001, **115**, 6596.
41 (*a*) Y. Morino, K. Kuchitsu and T. Shimanouchi, *J. Chem. Phys.*, 1952, **20**, 726; (*b*) K. Kimura and M. Kimura, *J. Chem. Phys.*, 1956, **25**, 362.
42 (*a*) W. S. Benedict and E. K. Plyler, *Can. J. Phys.*, 1957, **35**, 1235; (*b*) J. D. Swalen and J. A. Ibers, *J. Chem. Phys.*, 1962, **36**, 1914; (*c*) A. Rauk, L. C. Allen and K. Mislow, *Angew. Chem., Int. Ed. Engl.*, 1970, **9**, 400; (*d*) J. M. Lehn, Nitrogen inversion, in *Dynamic Stereochemistry, Fortschritte der Chemischen Forschung*, Springer, Berlin, Heidelberg, 1970, vol. 15/3, pp. 311–377.
43 (*a*) C. C. Wilson, *Crystallogr. Rev.*, 2009, **15**, 3; (*b*) H. B. Bürgi and S. C. Capelli, *Acta Crystallogr., Sect. A: Found. Crystallogr.*, 2000, **56**, 403.
44 (*a*) J. P. Gordon, H. J. Zeiger and C. H. Townes, *Phys. Rev.*, 1955, **99**, 1264; (*b*) J. P. Gordon, H. J. Zeiger and C. H. Townes, *Phys. Rev.*, 1954, **95**, 282.
45 M. Oxborrow, J. D. Breeze and N. M. Alford, *Nature*, 2012, **488**, 353.